D I P L O M A R B E I T

Correction of detector panel deflection for accurate intra-fraction motion monitoring in a radiotherapy linear accelerator

Ausgeführt an der
Fakultät für Physik
der Technischen Universität Wien

in Zusammenarbeit mit der
Universitätsklinik für Radioonkologie,
der Medizinischen Universität Wien

unter der Anleitung von

Univ.-Prof. Dr. DI Dietmar Georg
DI Dr. tech. Andreas Renner

durch

Katharina Heitger

Wien, December 14, 2021

Abstract

Radiotherapy is used to cure cancer by irradiating the cancerous tissue. One of the most common devices for treatment in radiotherapy is the linear accelerator (Linac). It has a treatment head and a detector that are both mounted on a gantry. The detector is used for patient position verification. Measurements have shown that during a rotation of the gantry the detector of the Linac experiences a displacement because of gravity. Due to the displacements the resulting images are distorted.
A foregoing work measured the displacement of the iViewGT™ detector used by the Elekta Versa HD, which is used for this work. In this work a corrective algorithm is established to correct the distortion in the images. For this, the measured displacements are taken into account to calculate the necessary transformation matrix, which is then applied to original images. Images acquired at the iViewGT™ at gantry angles 0° and 180° as well as a simulated image are then used to validate the algorithm. The application of this algorithm results in a decrease of the distortion in these images. The remained distortion in the simulated image is 20%. In a further work the corrective algorithm should be extended for the including kV-imaging system as it is expected to experience a deflection as well.

Acknowledgements

I would like to thank Univ.-Prof. Dr. DI Dietmar Georg of the Institute of Atomic and Subatomic Physics to open up the possibility of writing my thesis about this topic. I would also like to thank DI Dr. tech Andreas Renner. His door was always open, when I had questions or when I got caught up in a problem. Even during this time both had time to give me valuable comments on my thesis. Furthermore, I am grateful for my family who always had my back and had the patience to listen to me talking about the thesis. Finally, I want to thank my boyfriend, who supported me and helped me discuss different points of the algorithm.

Contents

1 Introduction and Motivation

Cancer is one of the main causes of death worldwide. There are different options to treat cancer, like surgery, chemotherapy or radiotherapy (RT). In RT ionizing radiation is used to kill cancer cells while minimizing damage to healthy tissue exploiting the so called therapeutic window. The therapeutic window is based on a different reaction of cancer cells and healthy tissue to radiation dose. RT treatments can be divided broadly into two categories: Brachytherapy and External Beam Radiotherapy (EBRT).
In Brachytherapy a radioactive source is placed near the tumor and therefore mostly inside the patient. In EBRT the radiation source is located outside the patient. The main device used for EBRT is the Linear Accelerator (Linac) [1, 2]. Linacs have a treatment head and a detector mounted on a gantry, which enables the treatment head and detector to be rotated around the patient. A Linac accelerates electrons to a high energy of several MeV, which can be used to produce X-Rays, formed by Coulomb interaction of the electron with a target material.
The electron or the X-ray beam is shaped in the treatment head using collimators to achieve conformity with the treatment volume [3]. The detector used with the referred Linac in this work is fixated on a retrievable arm. It is positioned at the opposite side of the treatment head and acquires images using the high energy treatment beam. It consists of a radiation sensitive layer, above which photons are formed by a scintillator plate [4].
Different studies showed that the detector experiences sagging and distortion [5, 6, 7, 8]. A foregoing work measured the dislocation of the detector of the Elekta Versa HD™, a Linac used at the Department of Radiation Oncology at the General Hospital of Vienna [9].
The displacements were measured using an inclinometer and an optical tracking tool. The tracking tool consists of infrared cameras and reflective markers. The reflective markers were mounted on the detector panel and at the isocentre position of the Linac as reference. Measurements were performed either for every 30° starting from 0° to 180° or for 0°, 90° and 180°with the detector arm extracted to the standard imaging position as well as to the fully extended position [9].
For medical purposes, it is essential to acquire images in high quality and without geometrical distortions. In radiotherapy, images are used during treatments for patient positioning, whereby geometrical accuracy is important. Therefore, the distortions have to be corrected. This can be either done by reinforcing the mount

of the detector, which has to be done by the manufacturer, or by establishing a correction algorithm to correct the distorted images after the acquisition.
The aim of this work is to provide a corrective algorithm which calculates a correction matrix for every gantry angle of the Linac. Multiplication of the matrix with the acquired image results in a corrected image.
Chapter 2 of the thesis gives the motivational and theoretical background for this work, such as cancer, radiotherapy or transformations. Chapter 3 describes the materials and methods used for developing the correction algorithm and the validation procedure. Chapter 4 describes the results and chapter 5 contains the final discussion of this work.

2 Background

2.1 Cancer

Cancer develops through mutations of healthy cells, going through stages from pre-cancerous cells to tumor cells. In general, the proliferation of cells is regulated by biochemical signals and different stages of the cell cycle. The amount of cells is controlled by death rates and proliferation rates of the cells. Tumor cells attain features during their development which result in fast proliferation and spread to various tissues [10].
In 2018 cancer caused the death in every eight men and one in every eleven women worldwide. The three most common cancers were lung, breast and colorectal, which appeared in the five most common cancer deaths, as well [11].
For a successful treatment of cancer early diagnosis and treatment are important. The primary goal of treatment is to cure the patient, but it can also be a goal to prolong the patient's life or to achieve a higher quality of life.

2.1.1 Cancer Treatment

Cancer can be treated in various ways. Available options are surgery, chemotherapy and radiotherapy as well as immunotherapy. These treatments can be applied in combination, as well [1, 12].
Typically, surgery is used with cancers which have not spread from the primary tumor site yet and early stages of this cancer. Chemotherapy is used, if the tumor cells have already spread throughout the body and, if the cancer is in an advanced stage [1]. Radiotherapy is used with early-stage and inoperable cancer and, if the location of the cancer is known and defined. Surgery has a good possibility of a complete cure while chemotherapy has a low possibility, but the life expectancy can be prolonged. While the outcome at locally well defined early-stage cancers treated with radiotherapy is the same as the outcome with surgery, the outcome at radiotherapy may be worse than surgery with advanced cancers [1]. Yet, the adverse effects on the body and the functional losses at radiotherapy are smaller. Which treatment will be applied is a patient specific question and will be answered individually by the physician [1].

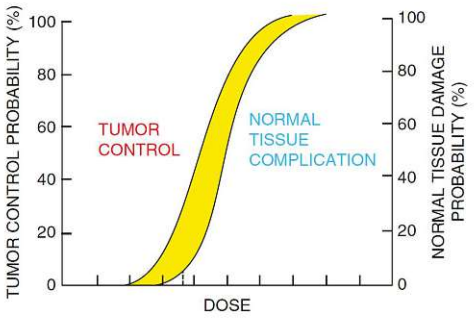

(a) The TCP and NTCP curves [10].

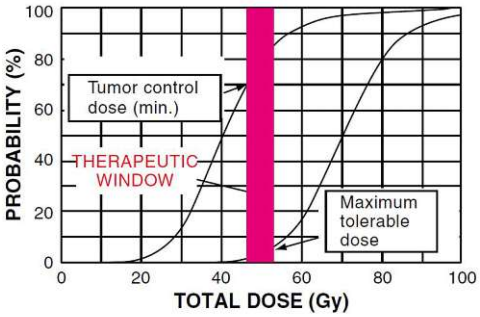

(b) The therapeutic window [10].

Figure 2.1: The tumor control probability and the normal tissue complication probability curves(a) and the therapeutic window determined by the TCP(left) and the NTCP (right)(b) [10].

2.1.2 Effect of Radiation on cancer cells

Tumor cells have chaotic growth, various sizes and chromosomes structures as well as different radiosensitivities. This knowledge is taken into account to achieve the aim of damaging the tumor cells while sparing the healthy tissue as far as possible. The therapeutic window, also called therapeutic index (compare Fig. 2.1), determines how the tumor control probability (TCP) is correlated with the normal tissue complication probability (NTCP) as function of radiation dose.
Factors affecting the TCP are, amongst others, the effect of oxygen, cellular type of tumor, dose rate and dose-time fractionation. TCP is linked to the dose and to the number of cells. The NTCP is depending on the number of fractions, the fraction dose, the total dose and the exposed tissue volume. Further factors affecting the NTCP are, amongst others, dose rate, dose-time fractionation, use of radioprotectors, and tissue radiosensitivity.
The aim is to pull the TCP curve to the left and the NTCP curve to the right as far as possible. Therefore, the two curves are further apart increasing the therapeutic window [10]. This leads to a range where tumor cells are damaged, while healthy tissue is less sensitive to radiation. Consequently if used in radiotherapy, this window can result into reduced side effects and local tumor control.

2.2 Radiotherapy

50-60% of cancer patients are treated with radiotherapy at any time throughout their treatment [13].
Radiotherapy can be divided into different categories considering various aspects:

- via aim:
  - curative
  - palliative
  - prophylactic radiotherapy
- via timing:
  - adjuvant radiotherapy, which is given after any kind of other treatment
  - neoadjuvant radiotherapy, which is given before any kind of treatment
  - postoperative radiotherapy,
  - preoperative radiotherapy
  - radiochemotherapy, which is the combination of radio- and chemotherapy.

In RT different types of radiation are used, which can be X-rays, α-, β-, γ-rays, protons or heavy ions [1, 14]. Some of the modes are EBRT, brachytherapy, radionuclide therapy, intraoperative therapy, intensity-modulated radiotherapy and image-guided radiotherapy [13], whereas the last two of them are part of EBRT [1]. EBRT will be explained in more detail in the next section.
In brachytherapy the radiation is applied via small, encapsulated radiation sources. They have a short range and are placed near the tumor. The radiation is then applied over a short period of time or over the lifespan of the radionuclide source. Types of implants are intravascular, intraoperative, intraluminal or surface. One advantage of brachytherapy compared to EBRT is, that the delivery of the dose is more localized. On the other side brachytherapy can only be used, if the tumor is small and the location well defined [2].

2.2.1 Clinical Workflow in Radiotherapy

After patient evaluation and the decision for RT is made, the steps of the workflow look as followed:

- Radiation treatment preparation: e.g. preparing masks or other immobilization devices
- Clinical treatment planning: e.g. determining the method of RT delivery
- Simulation: e.g. CT-scan and immobilization
- Dosimetric treatment planning: e.g. Definition of Target Volumes and Organs at Risk,

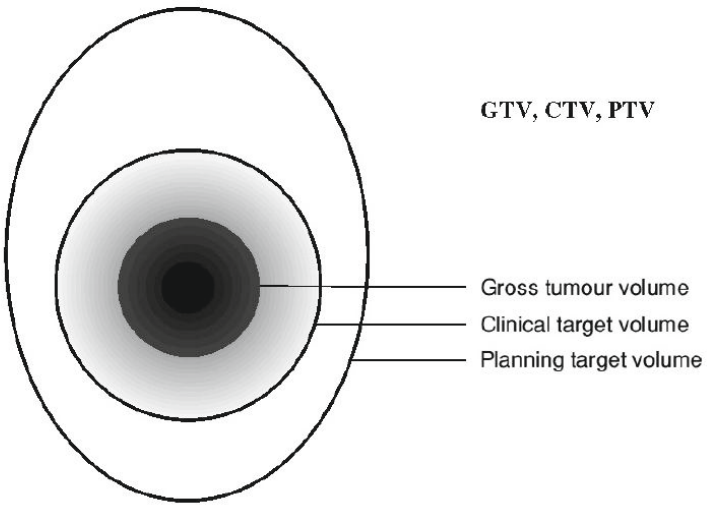

Figure 2.2: The GTV, CTV and PTV of the ICRU Report 50 [16].

- Pretreatment quality assurance and plan verification: e.g. Patient set-up
- Radiation delivery
- Radiation treatment management: e.g Toxicities monitoring
- Follow-up

Except the follow-up, the steps can be repeated [15].

2.2.2 Target Volume definition

For planning the treatment in Radiotherapy several ICRU reports (International Commission on Radiation Units and Measurements) apply. They define different volume terms of the tumor.
In ICRU 50 the Gross Tumor Volume (GTV), Clinical Target Volume (CTV) and Planning Target Volume (PTV) are defined (Fig. 2.2).

- The GTV is the visible tumor, which is palpable. Usually, the GTV has the highest tumor cell density, which has consequences for the dose.
- The CTV is the GTV plus a margin for a microscopic spread of the disease. It may be, that a CTV in a lymph node is present where no GTV exists. It is assumed, that the density of tumor cells is lower in a CTV than in GTV.

The CTV depends on the tumor characteristics as for example, some tumors are bound to anatomical barriers. If multiple imaging modalities are used, a possible displacement of the tumor in one modality relative to another modality can be corrected in the CTV. This is only possible, if the size and direction of displacement is known. Otherwise it has to be accounted for in the PTV.

- The PTV is the CTV plus geometric uncertainties. It considers organ motion, uncertainties in beam or patient set-up as well as tumor and patient movement. It is related to the isocentre of the Linac and therefore, it can reach the outside of the patient.

In ICRU Report 62 it is suggested to account for size or position variations for example due to a filled bladder, a so called internal margin. Furthermore, a set-up margin is suggested to account for uncertainties in positioning and planning. In this report the PTV results from the CTV plus the internal and set-up margin [16, 17, 18].
Another important definition introduced in ICRU report 62 is the Organ at Risk (OAR), which is a tissue characterized by its radiation sensitivity influencing the planning. A margin around the OAR assuring that little radiation is applied to the OAR is called Planning organs at risk volume (PRV) [13, 18]. Examples of ORs where a PRV is created is the spinal cord [16].
Furthermore, the treatment volume (TV) describes the volume which has the least probability of inducing complications and the irradiated volume (IV) is the volume getting a significant dose. The Conformity Index is the TV divided by the PTV [13].
In ICRU Report 83, which has the focus on Intensity-modulated RT (IMRT), the Remaining Volume at Risk (RVR) is introduced. It refers to irradiated volumina, which are not considered in other target volumina. With RVR unnoticed dose peaks can be detected in these volumina [19].
ICRU Report 91 corrects shortcomings of Reports 50, 60 and 83 regarding Stereotactic RT (SRT). In this report recommendations for image modality usage allowing accurate target volume delineation are given, while the basic ideas of GTV, CTV, PTV, OAR, PRV and ITV remain the same [20].

2.2.3 External Beam Radiotherapy

In External Beam Radiotherapy (EBRT) the radiation is applied from outside of the patients body. EBRT can be used with various treatment modalities and is performed using photon beams or particle beams. Photon beams use X-rays or gamma rays and particle beams protons or heavy ions.

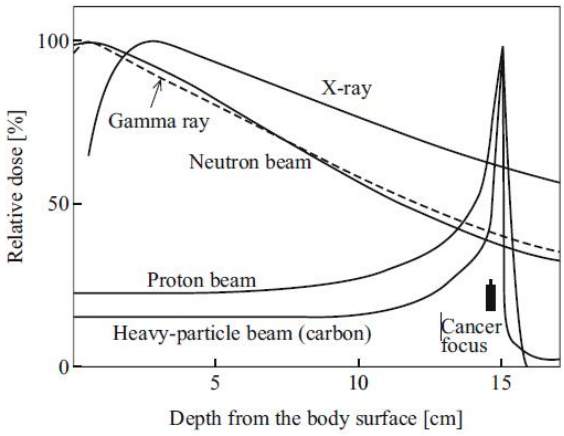

Figure 2.3: Depth-dose profiles of different types of beams projected onto the body [1].

Different beam types and their dose profiles are presented in Fig. 2.3. The curves show the energy loss of the particles. Heavy particle beams and proton beams have a narrow peak of the curve, called Braggs peak, while X-Ray beams show a wide maximum after entering the patients body and fading out afterwards.
Therapeutic rays can be generated by Linear Accelerators (Linacs), Co-60 units, Gamma knifes, Microtrons or cyclotrons. In Linacs electrons are accelerated and can be used to produce X-Rays. Linacs are described in the next section. A Gamma Knife is a therapy equipment based on gamma rays mainly used for lesions in brains. It has ^{60}Co radiation sources arranged in half circles build up that the rays converge at a single point in the lesion [1]. First, the source undergoes a beta decay, then the daughter nuclei emits gamma rays [3]. Microtons are modalities for EBRT combining characteristics of a cyclotron and a Linac. A cyclotron is an electron accelerator, which is build up from two semicircles. The electrons are accelerated in a spiral path. In the case of microtrons, there are racetrack microtrons and circular microtrons. In a circular microtron electrons accelerate through a microwave resonant cavity and travel through a spiral trajectory in a magnetic field. After passing the cavity the electrons gain energy. After accelerating the electrons follow an orbit with a bigger radius until they are extracted. In a racetrack microtron the magnets are two semicircles, the straight sides facing each other. The space between these semicircles allow for acceleration of the electrons. Further information can be found in [3, 21].

2.2.4 Conformal Radiotherapy

In conformal radiotherapy the beam is shaped to achieve high conformity to the tumor volume. Thus, the dose to the organs at risk is minimized. This radiotherapy technique is build upon target localization, treatment planning and dose delivery, all in 3D space. The localization of the tumor is facilitated by anatomical and functional imaging, like, CT, PET, MRI or ultrasound. Planning of treatment is either done by inverse planning or forward planning. Forward planning designs homogenous intensity beams, which are shaped to the geometric form of the target. In forward planning first, the irradiation method is determined, then the corresponding conditions are calculated. Contrary to this, in inverse treatment planning (ITP) the dose distribution is determined before the irradiation conditions are determined to match the dose distribution. ITP aims to decrease the dose received by organs at risk and improve the uniformity of the dose. For dose calculation the user specifies criteria for the doses of OARs and the target [1, 22]. Algorithms turn the chosen dose distribution into beam intensity maps which can then be applied by the Linac [23].

2.2.5 Intensity-modulated Radiation therapy (IMRT)

Intensity-modulated radiation therapy (IMRT) is based on ITP. To achieve adequate dose delivery to the CTV, the photon flux is modulated for sub-regions in the irradiated field. For calculation ITP is applied.
As the goal of IMRT is to decrease the dose to healthy tissues, the point in the patients body, where the maximum of the dose is applied, has to be controlled precisely throughout the treatment [1].
Simple IMRT treatments were made possible with wedges and physical compensators modulating the photon flux. Since the 1990s three dimensional imaging, ITP, quality assurance for dose delivery verification and dose delivery controlled by a computer made newer generations of IMRT possible [22].

2.2.6 Image guided radiation therapy (IGRT)

One difficulty in radiation therapy is reproducible patient positioning and precise tumor localization. Image-guided radiation therapy (IGRT), which supports IMRT as well, aims to ease this difficulty [1]. In IGRT, an image of the current position of the patient is acquired before and during treatment. More precise tumor localization allows for smaller margins in tumor planning. An ideal IGRT system should be able to acquire soft tissue images at the time of treatment and should be fast and simple for a high patient throughput. Furthermore, it has to be accurate regarding target definitions and has to be able to deliver a conformal

dose to the CTV [22].

2.2.7 Linear Accelerator (Linac)

Linacs are the most used radiotherapy equipment [1]. The principle behind generating rays for a Linac is similar to a common X-ray device. Electrons are accelerated by electrical fields. To achieve a high photon energy of several MeV needed for radiotherapy electrons are accelerated repeatedly by lower voltages in the accelerating waveguide (compare Fig. 2.4)[24]. Relevant components of the Linac for this work can be found in the treatment and equipment room of a Linac [25]:

- Gantry drum
- kV generator
- treatment table
- kV detector and source arm
- gantry arm and beam limiting device
- MV detector

Beam forming, which takes place up to the treatment head can be divided into following sections [3]:

- An injection system, which is a general electrostatic accelerator.
- A radio frequency power generation system. It produces a microwave, which accelerates the electrons in the accelerating waveguide.
- An accelerating waveguide, which is responsible for accelerating the electrons.
- An auxiliary system, which is not directly involved in the acceleration. It consists amongst others of a vacuum pumping system to produce vacuum in the RF generator.
- A beam transport system where bending magnets are used to transport the electrons from the accelerating waveguide to the target or the beam exit window.
- A beam collimation which consists of a primary collimator, a secondary collimator and optional a Multileaf Collimator (MLC), which is explained later on.
- A beam monitoring system

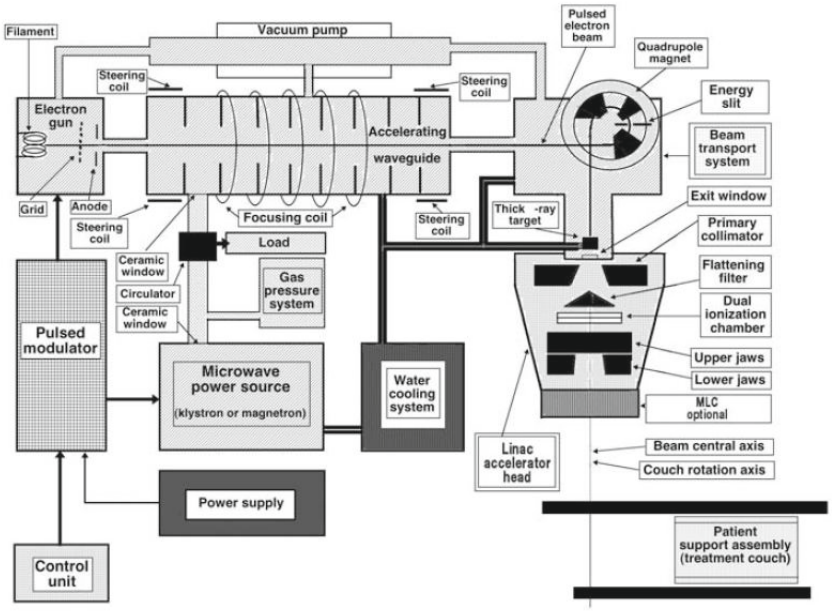

Figure 2.4: A diagram of a typical modern S band medical Linac [3]; shown are components and their connections

A simple accelerating waveguide has a cylindrical form with several discs that have holes at the centre and divide the waveguide into equal parts. These cavities make up the basic form of an accelerating waveguide. This waveguide is evacuated thus allowing the free propagation of electrons. The waveguide serves two purposes: Shaping of the appropriate electric field and distribution of the microwaves along the cavities [3].The elements of the accelerating waveguide have the properties of cavity resonators. The particles in the wall of the resonator can be excited to vibrations. Due to the shape and size of the apertures the electrical field lines are bent towards the middle resulting in a focused beam. The electrons can be accelerated via a travelling or a standing wave [24].

- **Travelling wave acceleration:** To meet the requirements of resonance, the cavities need to have the length of a quarter of the microwave. At resonance a charge distribution persists changing with the waves frequency. Thus, every forth cavity is suitable for acceleration at a given moment. Only the electrons, which are in a cavity of a maximal negative amplitude of the microwave are accelerated. The time needed by the electrons to travel to the next cavity is the same needed to get a maximal negative amplitude in the next cavity. This time is a quarter of the oscillation period of the

wave. Since the electrons are travelling with the speed of light c, they are accelerated every forth cavity.
With this technique, energies of 6 MeV to 18 MeV can be accomplished in typical Linacs. Higher energy require longer accelerating waveguides [24].

- **Standing wave acceleration:** Standing waves are build up when the wave is reflected at the end of the waveguide and the reflected wave constructively superimposes with the incoming wave, creating hills in every second cavity and valleys in every other. The electrons are accelerated, if they are at a hill at the same time as the electrical field strength reaches its negative maximum. In the valley electrons are not accelerated [24].

Usually, Linacs offering energies lower than 6 MeV have the accelerating waveguides situated parallel to the gantry rotation axis. Linacs offering electron energies higher than 6 MeV require beam transport, because of the additional length of the accelerating waveguides.
After the electron acceleration bending magnets are required to bend the accelerated electrons towards the target. The magnets have to bend the beam enabling it to collide with the X-Ray target or to leave at the beam exit window. Additional steering coils and focusing coils for focusing the electron beam are used in the electron beam transport with Linacs offering 10 MV and above 15 MV.
The accelerated electrons arrive in a pencil beam at the treatment head, which consists of various components for beam shaping [3]. The treatment head consists of

- Retractable X-Ray targets, enabling to irradiate with electrons and photons.
- Flattening filters, situated after the primary collimator, used for photon beams and flatten the photon beam.
- Scattering foils, with the retraction of the target and the flattening filter, scatter the pencil beam and electron beams are produced.
- Primary collimators defines the largest possible field size as an opening in conical form is build into a tungsten shielding block. The block is situated between the target and the flattening filter. The primary collimator is supposed to weaken the average X-Ray beam intensity to less than 0.1% of its original value. Thus, only the desired parts remain in the beam [3].
- Secondary collimators consist of four jaws, two upper and two lower jaws. They can be arranged to rectangular fields, with side lengths of a range of millimetres to 40 cm [3].

- Dual transmission ionization chambers monitor the beam output and the beam flatness.

- Wedges (optional): If the patient misses tissues after for example an tumor removing operation, an intentionally homogenous beam left at the treatment head can become inhomogeneous after entering the patients body, . This inhomogeneity can be compensated, amongst others, with wedges or compensating systems.
  Physical wedges can be differentiated into tertiary and build-in wedges. Tertiary wedges are configured for four different angles and have field sizes of 15 or 20 cm, while the field size in the non-wedge direction is limited to 40 cm. These wedges can also be put in any of the four directions. Built-in wedges are limited to one heel-to-toe direction.
  Physical compensators, as compensating systems, can be configured building upon a unique missing tissue. They are patient specific filters, which are placed between the treatment head and the patients surface. They can compensate along two planes [26].

- Multileaf Collimators (MLCs) (optional) consist of various leafs, which can be opened or closed and allow for field shaping. MLCs were first used in the 1960s. They differ in field size, leaf design and location depending on the manufacturers. One of the manufacturers, Elekta, has a MLC, with a field size of 40x40 cm^2. This system is reinforced by parallel diaphragms, which increase the attenuation of the MLCs.
  Another manufacturer, Varian, has various MLCs. One of it has 120 leafs, where the inner leafs are narrower than the outer leafs. The inner leafs therefore allow for shaping in more detail. Both, inner and outer leafs have 20 cm thickness each.

- Other components for field shaping are asymmetric jaws blocking regions from radiation and thus reducing the dose in these regions. They are able to open and close independently from each other providing an attenuation. They are used for breast, head, neck, craniospinal and prostate cancer [26].

- A light field describing the treatment area.

- A range finder projects a centimetre scale, which is used to place the patient at the correct vertical distance from the isocentre.

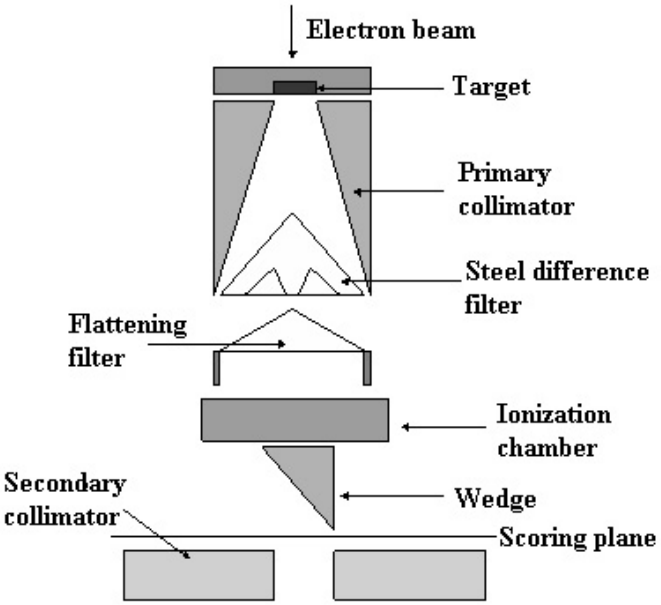

Figure 2.5: A schematic representation of filters of a Linear Accelerator [27]

2.2.8 X-ray devices

X-rays are used both for diagnostics and treatment in radiation oncology. In this section devices for treatment are considered. Superficial and orthovoltage X-rays are between photonenergies of 10 keV (kiloelectron Volts) and 100 keV, and between 100 keV and 500 keV, respectively. Both are produced in X-ray units. X-rays which are produced with electrons having a kinetic energy higher than 1 MeV (Megaelectron Volts) are called MV (Megavoltage) X-rays and are produced in Linacs or sometimes in betatrons or microtrons. keV and MeV represent the energy spectrum of X-rays, which are excited with a specific X-ray voltage given in kV (kilovoltage) and MV.
In the range of 10 kV to 150 kV the photons are produced 90° to the acceleration direction. In the range of 1 MV to 50 MV the production occurs in the direction of the acceleration of the electrons [3].

2.2.9 Attenuation of X-ray in tissue

X-rays interact with tissue via the photoelectric effect, Rayleigh scattering, Compton scattering and pair production [28, 29].
Photoelectric effect: The photon interacting with an electron is absorbed by the electron, which then leaves the atom. This is most probable when the energy of the X-ray equals the binding energy of the electron, the probability decreases

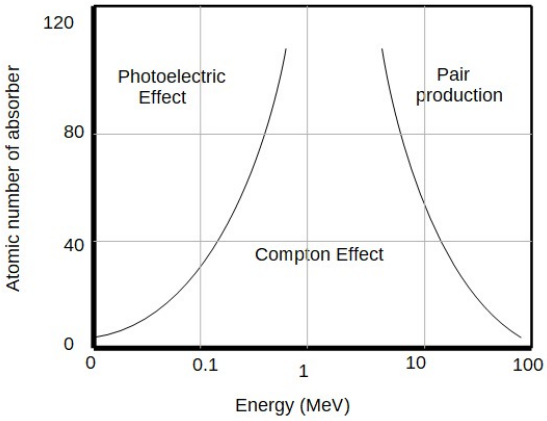

Figure 2.6: Different Types of Interaction with matter depending on energy and atomic number of the absorber.

as the energy of the X-ray increases and it is not possible if the energy of the X-ray is less than the binding energy of the electron. The result is a positively charged ion and an electron. The place of the separated electron in the ion is filled by an electron from a higher shell, which results in characteristic radiation. In human tissue this characteristic radiation will be absorbed immediately as it has low energy.

Rayleigh scattering: No exchange of energy takes place as the incident photon is scattered elastically as it interacts with an electron. It is most frequent in X-rays with low energy hitting materials with a high Z number. In the case of X-ray imaging it is less probable.

Compton scattering: It occurs when the binding energy of the electron is less then the energy of the X-ray and is therefore most probable in the outer shells of an atom where the binding energy is low. The interaction results in the initial photon being inelastically scattered reducing its kinetic energy, a new formed ion and an electron from the participating atom. It is the most likely interaction to happen in diagnostic imaging and in radiation oncology [28].

Pair Production: An incident photon transforms into a positron and an electron. The electron looses its energy by absorption effects. The positron travels through matter, ionizes atoms and slows down until it collides with an electron in an annihilation process. This results in two photons which propagate in opposite directions with a kinetic energy of 0.511 MeV each. These photons interact via photoelectric effect or Compton scattering. Pair Production is possible above 1.022 MeV and increases with increasing atomic number of the tissue. Above 10 MeV Pair Production occurs more often than Compton Scattering. [29]

According to Lambert-Beers-Law the intensity of an X-ray beam travelling through homogenous tissue of the thickness δx and an initial energy of I_0 is given by

$$I_x = I_0 e^{-\mu \delta x}. \tag{2.1}$$

μ is the linear attenuation coefficient and is the sum of probabilities of all interaction types and is specific for each material and photon energy. In the case of inhomogeneous tissue with n different μ the intensity is calculated by

$$I_x = I_0 e^{-\sum_{i=1}^{N} \mu_i \delta x_i}. \tag{2.2}$$

In medical imaging each pixel has a different greyvalue depending on the attenuation of the intersecting X-ray beam with the detector as every tissue which is travelled through by the beam has a different composition [28].

2.3 Imaging in Radiotherapy

It is important to know the exact localisation and extent of the tumor as well as the attenuation of the tumor and its surrounding. For this reason different imaging modalities, like Computer Tomography (CT), Positron Emission Tomography (PET) or Magnetic Resonance Imaging (MRI) are used.
MRI and PET will be discussed here, CT will be discussed in more detail later on, as it is the most widely used modality for treatment planning.

Magnetic Resonance Imaging (MRI) uses specific magnetic properties of hydrogen atoms in the body for imaging. An MRI system consists of a main magnet, gradient coils and a high-frequency system. In the bore of an MRI device the patient can be moved on a patient couch.
In the context of MRI atomic nuclei can be described as bar magnets. An MRI system has a strong magnetic field which aligns these magnets. As a short radiofrquency pulse is applied, the magnetization of the hydrogen atoms is turned away from the direction of the magnetic field onto the transverse plane. This movement sends out a signal. Interactions between nuclei lead to phase differences which lead to a decrease in this signal. Furthermore the magnetization realigns with the magnetic field. The time it takes to realign (T1) and the time the signal of the decreasing signal takes to decrease to approx. 37% (T2) are taken into account for imaging [30, 31, 32].

Positron Emission Tomography (PET) is a functional imaging device which can visualize biological processes using radioactive tracers, which are injected into the patients body. One frequent used tracer is ^{18}F-FDG, which is a glucose-analogue. In contrast to other modalities, like CT where the radiation source for

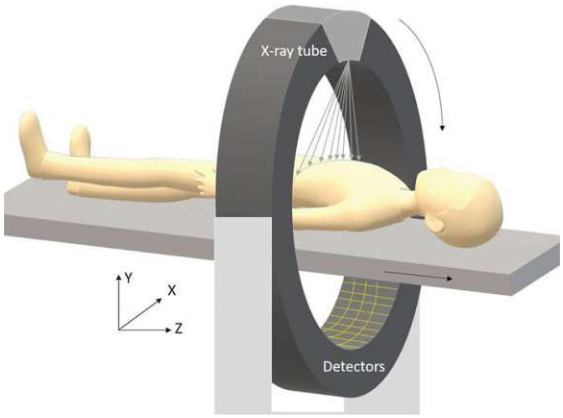

Figure 2.7: A schematic image of a CT. Shown are the X-ray tube and the array of detectors.The X-ray tube and the array of detectors rotate around the patient, while the patient couch is moved along the z-axis to obtain a 3D-image. Taken from [28].

imaging is outside the patient, the source for PET is inside the patient. Following a β^+-decay a positron is emitted inside the patients body. After annihilation with an electron a pair of 511 keV photons is produced. Travelling in opposite directions these photons can be detected at a PET ring detector, after which an image can be reconstructed . A PET scanner consists of a ring of detectors which detects the annihilation photons [33].

2.3.1 Computed Tomography (CT)

A modern clinical CT scanner consists of a gantry on which an X-ray tube and on the opposite side, an arched detector are mounted, as it is shown in Fig. 2.7. Additionally, a patient couch is used for positioning the patient. This couch is used to move the patient along the z-axis to obtain a 3D image as well [32].

The first CT generation consisted of a detector and a tube which translated and rotated around the patient to form one CT-slice. This was repeated for every necessary slice. Up to the third generation the number of detectors placed beside each other grew and formed an array of detectors. The translating motion became unnecessary and only the rotation remained.

In the forth generation the whole ring was covered with detectors addressing the instability of moving detectors as well. Due to pragmatic and economical reasons, as well as the number of detectors necessary, this generation is less common than the third generation [28].

During rotation of the X-ray tube and the detector, the attenuation of the X-ray fan-beam is measured. The result is a sinogram, which is used to reconstruct the

image. For every beam path the summed up attenuation is obtained. The resulting CT image consists of a distribution of the attenuation coefficients visualized in greyvalues [28, 32]. The reconstructed pixels are given in Hounsfield units (HU), which are scaled as

$$HU = \frac{\mu_{tissue} - \mu_{water}}{\mu_{water}} * 1000. \tag{2.3}$$

Air has a CT value of -1000 HU and water has a CT value of 0 HU. With this, every pixel value can be assigned to a known scale, which leads to a consistency of the assignment of CT values to different organs During reconstruction the CT values are calculated, which have to be consistent with the attenuations of the respective beam paths.

The raw image data is a sinogram, which consists of a matrix. In this matrix rows correspond to projections angles and the columns correspond to the array of detectors. There are different methods of how to reconstruct the final image out of a sinogram. Some of them are back projection and filtered back projection. The simpler Back Projection is explained here, while others can be found in [28]. In Back Projection every projection angle is considered separately first. Every pixel along each beam in a projection angle is assigned an equal value. For example the pixels of a beam having value a with b participating pixels are each assigned the value a/b. The summation of these results of every projection angle yields the reconstructed image. This Back projection method is simple to implement, but results in blurred images, which can be removed with filtered back projection [28]. Nowadays, the modes of a CT scan can be either axial or helical. Axial scans were the original mode and are still in use. Here, the detector and the tube rotate around the patient without any translation along the patient. The patient couch is standing still as well. Therefore, the area which can be covered by one scan is limited by the width of the detector. The slices are computed at specific positions depending on the detector. If a scan has to be wider then the width of the detector, the patient couch moves the width of the detector after a rotation, so that the next axial scan can start.

At a helical scan the patient couch moves continuously while the detector and tube rotate and scan the body. Due to the constant motion there is no specific location at which slices are reconstructed but any location can be chosen to be visualized as a slice after the scan is completed. The obtained data from the scanned volume is used to reconstruct subsequent images.

For cardiac scans even the scan times of initial third generation CTs are too long to capture sharp images of the heart. The solution involves the rhythm of the heart and is called the 'step-and-shoot-technique'. The scans are timed with the help of an ECG (Echocardiogram) as the patient is irradiated at a specific point of the heart cycle. Then the patient couch is moved and the patient is scanned again at the same phase of the heart cycle. This is done until the whole heart is

scanned. Another solution, 'retrospective gating', involves inquiring data during several heart cycles, thus containing increased radiation compared to the 'step-and-shot-technique'. The data acquired at the wanted phase in a heart cycle is selected and reconstructed. Nowadays, scanners have a larger width covering the whole heart and a faster rotation time which results in clear images [28].

2.3.2 Cone Beam computed tomography (CBCT)

CBCT can be used to verify the patient position and thus the tumor position when the patient is placed on the treatment table at the Linac. In CBCT a flat panel detector and an opposing X-ray source are connected with the Linac gantry. The whole CBCT system can rotate around the patient table and thus enables to acquire various planar images as well as reconstruction of volumetric data. The images can be acquired by using either a kV or MV cone beam. The X-ray tube for the kV beam is mounted at 90° to the treatment head of the Linac, whilst a flat panel X-ray detector is at the opposite side of the X-ray tube [22].

For using a MV beam no additional dose is needed, as the beam line of the Linac is used. For imaging the detector which is already mounted for the Linac is utilized [22].

2.3.3 Electronic Portal Imaging Device (EPID)

Electronic Portal Imaging Devices (EPIDs) are used for image acquisition in RT using the therapeutic beam. An EPID is mounted on the opposite side of the treatment head, allowing imaging at every gantry angle. The first EPIDs were video-based or matrix ionization chamber-based systems, whereas the subsequent ones are active-matrix flat-panel imagers or amorphous silicon flat-panel detectors. The Linac referred to in this work, Electa Versa HD uses an amorphous silicon flat-panel detector as an EPID. Arrays, which form the pixels are made from hydrogenated amorphous silicon. Each pixel of this array consists of a photodiode and a transistor. In front of the photodiode a metal plate and a phosphor screen are situated, converting X-rays into light. The photodiode converts the light into electron-ion pairs which are collected by a storage capacitor to be read out.[34]

2.4 Image Transformations

Transformation matrices are used to change the size, orientation or shape of an image. This means transformations can translate, rotate, reflect, scale or shear objects and shapes [35].

Geometric transformations appear, when the geometry of an image changes, but the values of the image's pixels them-selves do not. The following equations are given in 2D space, but can be extended to the 3D space.

Translation is the transformation shifting the geometry with a given offset displacement horizontally and/or vertically. The equation for translation is:

$$\begin{bmatrix} x' \\ y' \end{bmatrix} = \begin{bmatrix} x \\ y \end{bmatrix} + \begin{bmatrix} \Delta x \\ \Delta y \end{bmatrix} . \tag{2.4}$$

Scaling is a transformation to zoom in or out, or to make the object bigger or smaller. With S_x and S_y as the scaling factors, the equation for scaling is as followed:

$$\begin{bmatrix} x' \\ y' \end{bmatrix} = \begin{bmatrix} S_x & 0 \\ 0 & S_y \end{bmatrix} \cdot \begin{bmatrix} x \\ y \end{bmatrix} . \tag{2.5}$$

For rotation the desired angle θ for rotating the image counter clockwise is needed. With this angle given the equation is:

$$\begin{bmatrix} x' \\ y' \end{bmatrix} = \begin{bmatrix} \cos\theta & \sin\theta \\ -\sin\theta & \cos\theta \end{bmatrix} \cdot \begin{bmatrix} x \\ y \end{bmatrix} . \tag{2.6}$$

The difference in shearing to translating is that the horizontal and vertical shift is not the same. For shearing the equation is as followed:

$$\begin{bmatrix} x' \\ y' \end{bmatrix} = \begin{bmatrix} 1 & Bx \\ By & 1 \end{bmatrix} \cdot \begin{bmatrix} x \\ y \end{bmatrix} . \tag{2.7}$$

These transformations can be combined by multiplying the matrices [36].

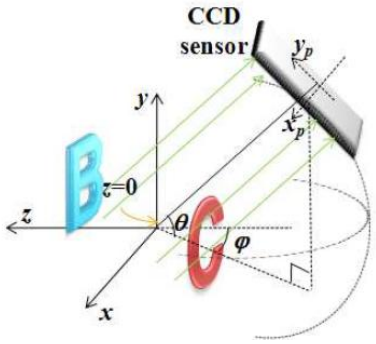

(a) Angular orthogonal projection taken from [37]The rays are parallel and the image plane is tilted.

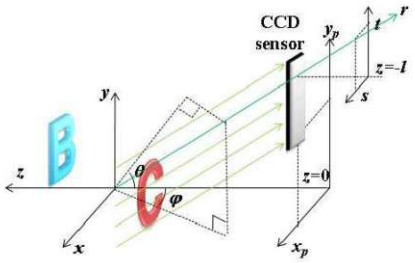

(b) Orthographic projection taken from [37] The rays are parallel and the image pane is not tilted.

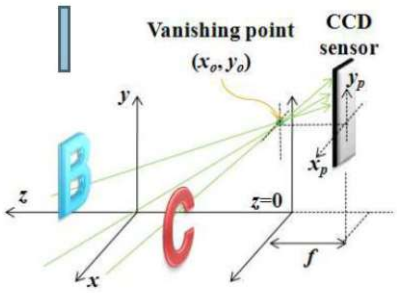

(c) perspective projection taken from [37] Rays assemble at one point

Figure 2.8: Different projection geometries taken from [37].

2.5 Projection geometry

The geometrical relationship between 3D-space and an image plane is called perception geometry. There are mainly three different geometries, shown in Fig. 2.8. First, there is angular orthogonal projection geometry. The rays are parallel to each other, the image plane is tilted with an orthogonal vector having angles ϕ and θ.
The orthographic projection geometry has parallel rays as well, but the image plane is not tilted.
Finally, the perspective projection geometry has rays assembling at one point [37]. At perspective projection geometry it is assumed that the pixels in the image plane

are evenly distributed. This projection geometry is present for example with pinhole cameras [38].

2.5.1 Digitally Reconstructed Radiograph

A digitally reconstructed radiograph (DRR) is reconstructed from a 3D CT-scan resulting in a 2D image simulating a planar X-Ray image [39]. As a projection geometry a perspective projection, described in the previous section 2.5 can be used. One method of reconstruction is described by Sherouse et al [40]. In their work a 3D CT data set is placed virtually in a rayset that comes from a virtual source and passes through the data set onto a virtual detector plane. The intersection of a ray with the detector plane marks one pixel of the DRR. The different angles of the gantry can be achieved by moving the source and the detector accordingly. This method can be varied in the details of the implementations [40, 41].

3 Material and Methods

The aim of this work is to develop a corrective algorithm for image distortion caused by the tilt of the detector arm mounted to the gantry of a Linac. The work is based on measurements of the detector tilt from a previous work [9]. It was found that the arc of rotation of the real detector is in the shape of an ellipse, whereas the arc of rotation for an ideal detector would be in the shape of a circle. The algorithm computes the transformation matrix using the real and ideal detector position obtained from the detector tilt measurements. This matrix is then applied onto an acquired image for correction.
Every step of this program is tested and the program is validated by measured and simulated images.

3.1 Elekta Versa HD

Elekta Versa HD is a Linac by the Swedish company Elekta. The Versa HD is capable of delivering photon and electron beams. The maximum field size is 40x40 cm^2 [42].
The Linac consists, amongst others, of a voltage stabilizer, a gantry drum, a reeling interface cabinet and a kV generator in the equipment room. The gantry assembly contains a gantry drum including a gantry arm. This arm consists of the waveguide to deliver the radiation to the beam limiting device. [25] On the opposite side of the gantry arm the detector arm leading to an EPID„ the iViewGT™, is situated.

3.1.1 iViewGT™

On the gantry, as an EPID, the iViewGT™ system, shown in Fig. 3.1, is mounted [43]. iViewGT™ is a system for RT imaging using the MV treatment beam. Thus, no additional dose is necessary.
An image is detected via a scintillator plate to transform the high energy photons into visible light. It is attached to an amorphous silicon detector, which consists of amorphous silicon diodes as a two dimensional photodiode array and forms with 1024x1024 pixels the radiation sensitive layer. The signals are then transmitted from the amorphous silicon diodes to a computer framegrabber. At the PC the image is processed and displayed.

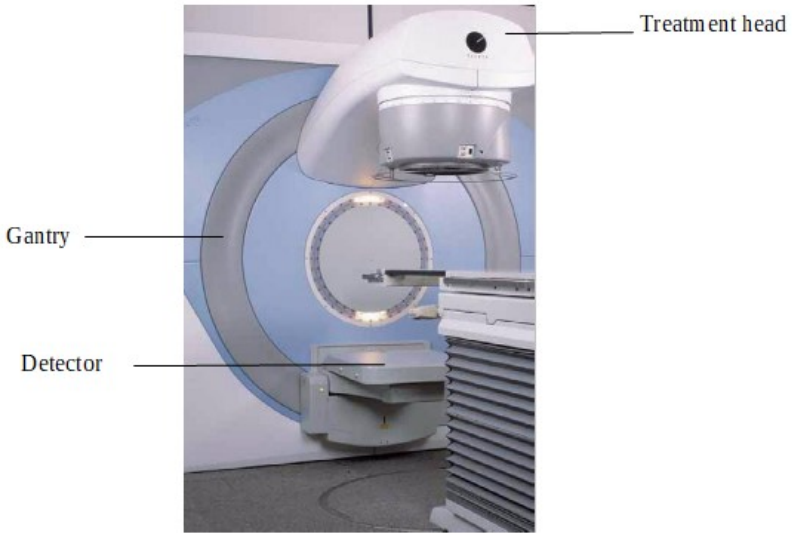

Figure 3.1: The iViewGT™ detector mounted on a Linac [43]. is the treatment head, the gantry and the iViewGT™ detector.

The system does not affect the functioning of the accelerator. Instead it waits until radiation is detected. Then the software starts to collect the data. The possible modes are single-exposure, double exposure (only for non-IMRT systems), multiple-exposure (only for IMRT systems) and movie exposure.
The EPID is supported by a retractable arm. The arm is responsible for bringing the detector in the desired position for image detection. The standard imaging position is the central axis position, but can be moved to treatment fields aside from the isocentre [43, 4]. The fully extended EPID is 115 mm away from the isocentre [44]. The points of the EPID given in Fig. 3.3 are 205 mm away from its centre, the radiation sensitive layer has a field size of 41x41 cm^2 [45], whereas the acquired images have dimensions of 1024x1024 pixels. Consequently, an average of 2.49 pixels are visualized on an area of 1 mm^2 on the detector.

3.2 Matlab

The algorithm established in this work is written in Matlab (developed by Mathworks®). Matlab is popular for signal and image processing [46]. The program enables to write classes, functions and scripts. It is designed for matrix-manipulation, which is used in this work. Furthermore, it allows for visual representation of the results and has extensive documentation.

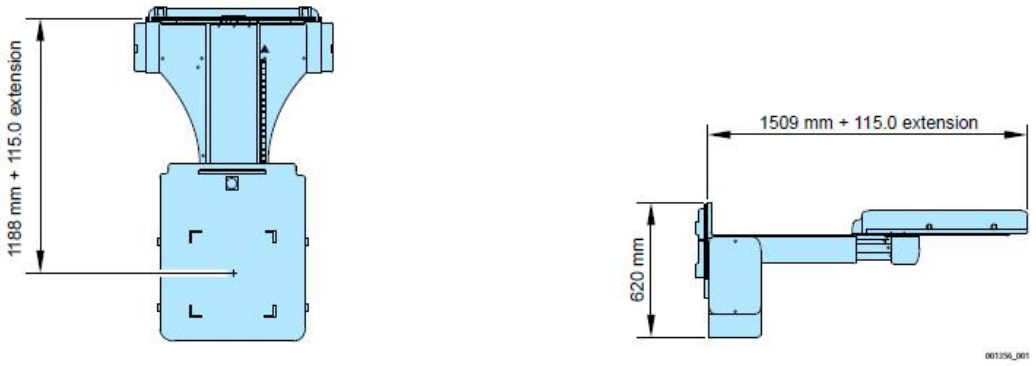

Figure 3.2: The dimensions of the iViewGT™ detector at the isocenter and fully extended position [44].

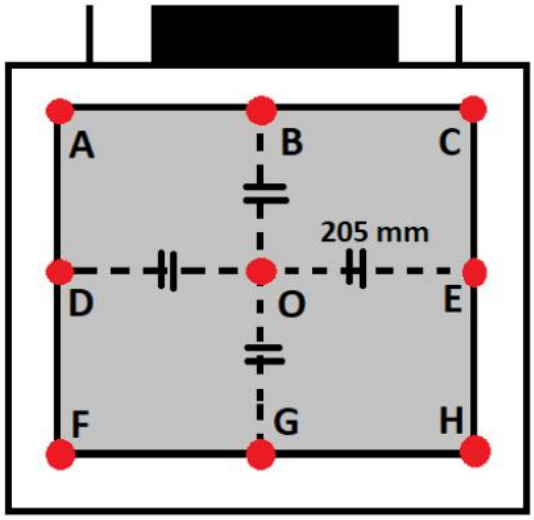

Figure 3.3: The points of the detector used for calculation of the detector position in this work and their distances to each other. In this figure the detector arm leading to the gantry is symbolized by the black area. Taken from [9].

3.3 The corrective Algorithm

For this corrective algorithm following assumptions are made about the gantry and the detector arm system:

- the fixation of the detector on the gantry makes a perfect circle rotating around the patient;
- the detector itself does not bend; the whole system (detector arm and detector) does tilt downwards under the influence of gravity

For working with points in their real and in their ideal position two coordinate systems have to be established, shown in Fig. (3.5). The gantry coordinate system, used in a previous work [9] assumes a 3D coordinate system with its origin in the isocentre, the x-axis extending from superior to inferior, the y-axis from right to left and the z-axis from posterior to anterior as shown in Fig. 3.4. All directions are from anatomical point of view of a patient laying on its back with the head towards the gantry.
Additionally, a new coordinate system, the detector coordinate system, is established with its origin at the fixation point of the detector arm on the gantry. This coordinate system is dependent on the gantry angle (Fig. 3.5). It is used for calculating the transformation matrices. The calculation of real and ideal detector positions of all gantry angles is explained in chapter 3.3.2.
The transformation matrix is then computed, which is described in chapter 3.3.3. The resulting matrix is stored to be applied on an image later on. The structure of the developed algorithm is visualized in Fig. 3.6.

3.3.1 Input data

The ideal detector positions were already calculated for gantry angles 0°, 90° and 180° in the previous work [9] and are listed in table 3.1. The points for other gantry angles have to be interpolated using interp1(). The function interp1() in Matlab returns values of a 1D-function at specific points. As an additional input parameter a method can be specified, which determines how the interpolation is performed. This method can be amongst others 'linear', which performs linear interpolation or 'cubic', which performs cubic convolution. In this program 'cubic' was used.
The points are named A-H and O. O is the detector centre and A-H are points on every edge and in the middle of the sides of the detector, as seen in figure 3.3.
For the calculation of the real detector positions the distance of the isocentre to the detector centre measured for gantry angles 0°, 30°, 60°, 90° 120°, 150° and 180° are taken from [9]. They are listed in table 3.2.

0°:

Point	x(mm)	y(mm)	z(mm)
O	0	0	-580
A	-205	-205	-580
B	-205	0	-580
C	-205	205	-580
D	0	-205	-580
E	0	205	-580
F	205	-205	-580
G	205	0	-580
H	205	205	-580

90°:

Point	x(mm)	y(mm)	z(mm)
O	0	-580	0
A	-205	-580	205
B	-205	-580	0
C	-205	-580	-205
D	0	-580	205
E	0	-580	-205
F	205	-580	205
G	205	-580	0
H	205	-580	-205

180°:

Point	x(mm)	y(mm)	z(mm)
O	0	0	580
A	-205	205	580
B	-205	0	580
C	-205	-205	580
D	0	205	580
E	0	-205	580
F	205	205	580
G	205	0	580
H	205	-205	580

Table 3.1: Ideal Detector positions for 0°, 90° and 180° calculated in [9] used as basis for further calculations.

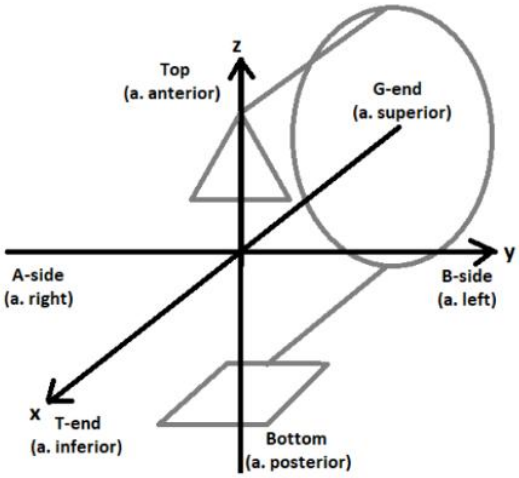

Figure 3.4: The coordinate system used in the previous work and in this work as gantry coordinate system. It is used for calculation of the points of the detector. Taken from [9].

Gantry Angle in degrees	Distance isocentre to detector centre (mm)
0	590
30	591
60	589
90	587
120	586
150	584
180	584

Table 3.2: The measured distances from isocentre to the detector centre. Taken from [9].

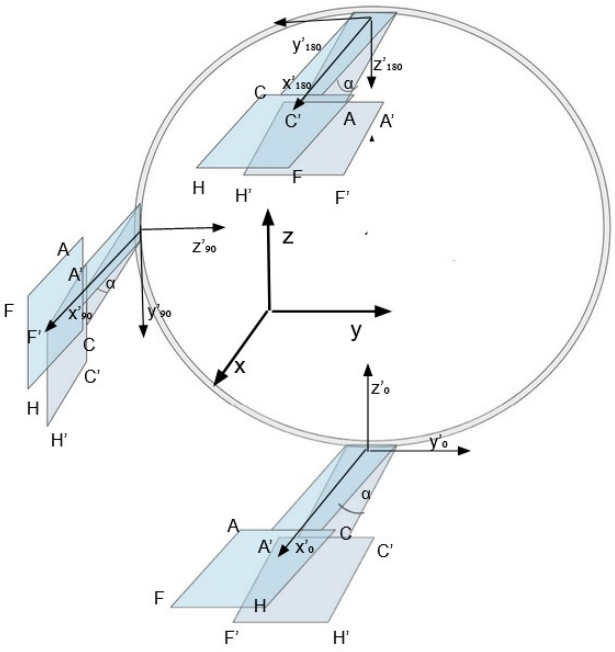

Figure 3.5: Coordinate systems used in the correction algorithm. Coordinate system (x,y,z) is the gantry coordinate system with its origin at the isocentre and is the same as in [9]. Coordinate system (x',y', z') is the detector coordinate system which is depending on the current gantry angle. Its origin is at the fixation point of the detector arm on the gantry. Points A - H are the ideal points a detector without tilt, points A'- H' are the real points of the detector, which are deflected by angle α from the ideal position.

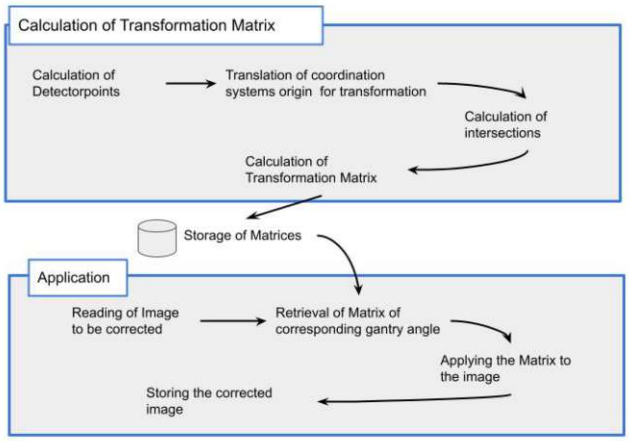

Figure 3.6: The structure of the algorithm. First, the transformation matrices are calculated and stored. Then the necessary transformation matrix is retrieved and applied onto an image.

3.3.2 Calculation of the detector position

For the calculation of the points of the ideal detector position the points A-H are calculated with the interpolation function of Matlab interp1(). As input the pre-calculated points at 0°, 90° and 180° in table 3.1 are used. Since the ideal detector moves within an ideal circle, the point O is determined using the formula of a circle. Again, the pre-calculated points from table 3.1 are used as input parameters.
Furthermore, the new coordinate system having its origin at the fixation point of the detector on the gantry is established. The ideal points are transformed from the gantry coordinate system to the new detector coordinate system.
For the calculation of the real detector positions the values listed in table 3.2 are taken into account. With these values the detector centre and the experienced detector tilt are calculated. As it is assumed that the detector itself does not bend, the other points are calculated using the detector geometry, as shown in Fig. 3.3.
The same points are calculated for the detector at the extended position, 115 mm away from the isocentre.

3.3.3 Calculation of the transformation matrix

Both, the ideal and real points of the new coordinate system are taken into account for this calculation. First, lines between the real Points A,C, F, H and O as shown

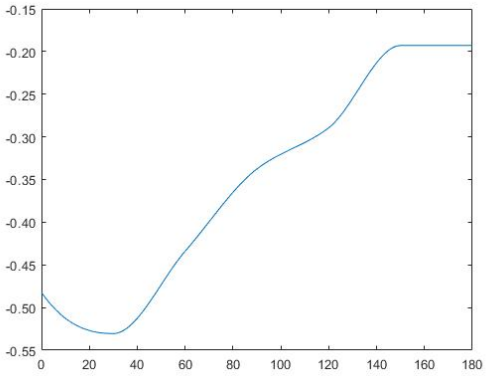

Figure 3.7: The calculated detector tilt for gantry angles 0° to 180°. It is calculated using the points of the ideal and real detector positions.

in Fig. 3.3 and the source are created. The lines are then used to calculate their intersections with the ideal detector plane. These intersection points limit the area with image information on the ideal detector plane. The intersection points and the real points limiting the detector are then converted from 3D to 2D points as a projection. These 2D points serve as input for the function fitgeotrans() from Matlab, which returns a calculated transformation matrix [47]. fitgeotrans() accepts as a further input parameter a method as well. In this case 'projective' as a method is chosen. The documentation states, that this method should be used when the image appears to be tilted. The final transformation matrix is stored with the respective gantry angle and with a boolean variable, if the detector is in the fully extended position or not.

3.3.4 Applying the matrix

The measured image is loaded into the program and an users input is requested for giving information about the filepath of the image and the extended position. Then, the appropriate transformation matrix is loaded into the script and is applied onto the acquired image. The matrix is applied with the function imwarp() from Matlab [48]. As interpolation methods three different methods (linear, cubic, nearest neighbour) are available. Here cubic interpolation is used.

3.4 Validation

3.4.1 Testing the code

The algorithm can be divided into different sub-programs. First, the ideal O-Points are calculated for every gantry angle, then the other points of the detector. Points are converted to 2D by projection. Then the transformation matrix is calculated with the aid of 2D points. All these sub-programs are tested separately, whereat the calculation of the transformation matrix depends on the calculation of the points.
For calculation of the ideal O-Points the known points for three gantry angles are used. First, the calculated O-points of these gantry angles are compared to the given points. The ideal detector centres from 0° to 180° are plotted to examine, if they result in a semi-circle. The points A-H are tested as well. Visual inspection is used to check, if the calculations return reasonable results. Additionally, the real and ideal detector points at the same gantry angle are plotted together.
The resulting transformation matrix is tested by the program validation.

3.4.2 Program Validation

The program is validated in two ways. On one hand, a simulated image is used assuming a tilted detector. On the other hand the program is validated by two images measured at the Linac, one at a gantry angle of 0° and one at a gantry angle of 180°. With the help of a self-written simulation program an image acquisition by a tilted (real) detector is simulated. A plane is stretched out with its centre in the isocentre to mimic a flat object and visualize the image distortions caused by the tilt of the detector. As an input the same detector positions which are calculated for a gantry angle of 0° are given to the program. Consequently, the image simulated with the tilted detector can then be used as an input for the correction algorithm. The differences between the simulated image with the corrected image can thus be compared. For simplification, the edges of this plane are considered which indicate the distortion and the correction of this distortion.

For the second method of validation the images are acquired using the Elekta Versa HD™. Five spheres (steel-ball bearings), each with a diameter of 10 mm, are placed on the treatment table with the detector being at the isocentre position. One sphere is placed in the isocentre, the other four at the edges of the treatment field. The set-up is shown in Fig. 3.8. The images are taken at gantry angle 0° and 180° (Figure 4.3a and 4.3b). In Matlab these two images are turned into binary images and the coordinates of the centre of every sphere is calculated. Assuming no tilt at any place the spheres should be at the same place and there should not

Figure 3.8: The Set-up of the measurements of the spheres. The spheres are situated at the four edges and at the centre of the detector.

be any visible differences. The images are visually compared with the function imfuse(). As an input the corrected images taken at gantry angle 0° and 180° are used, the method 'diff' serves as an additional input. Using this method the function returns a difference image. Additionally, the smaller images are put into an empty matrix the same size of the bigger images, but with the centre at approx the same position as the centre of the bigger images. Having the same size, the images are subtracted from each other. This way, negative and positive differences can be seen. Moreover, the coordinates of the centres of the spheres are calculated and compared to the coordinates computed before correction.

4 Results

This chapter contains the results of the code validation, described in chapter 3.4.1. and the results of the validation of the program itself, described in chapter 3.4.2.

4.1 Testing the code

Fig. 4.1 shows the ideal detector centres for gantry angle 0° to 180°. The ideal points plotted in blue show a semi-circle.

In Fig. 4.2 the real and ideal points A-H and O of the detector in the new coordinate system at a gantry angle of 0° are plotted. Recognizable is the tilt of the detector and that the detector does not bend. This was done for several gantry angles to show the results of the calculations of the points. With this, possible outliers would be visible.

4.2 Program validation

For initial validation an image acquired at gantry angle 0° is simulated and the edge points of this image are taken into further consideration. The image is considered having 5000x5000 pixels. After applying the transformation matrix the image has 4958x4943 px. The positions of the edge points before and after correction are listed in table 4.1. The experienced distortions before and after correction are listed in table 4.2 showing an distortion of (10/0)px before and an distortion of (2/0)px after application of the correction algorithm.

Two images of five spheres acquired by the Linac are compared, shown in Fig. 4.3a and Fig, 4.3b, both having 1024x1024 px. The centres of the spheres are calculated and are listed in table 4.3 as coordinates in the images. This means that each integer value given as a coordinate refers to one pixel in the image.

One of the spheres in Fig. 4.3b (denoted as B) is close to the frame of the image, this sphere is not recognized by Matlab as an individual object at the image taken at the gantry angle at 180°, but is counted to the frame. Consequently, only four objects are recognized for the image taken at a gantry angle of 180° and five objects are recognized for the image taken at a gantry angle of 0°, shown in Fig.

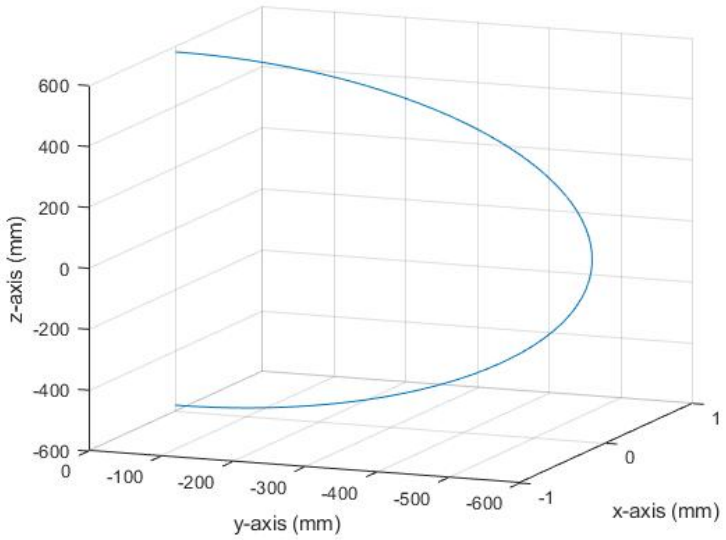

Figure 4.1: The ideal O-Points plotted as a semi-circle in Matlab, as the ideal arc of rotation is a circle.

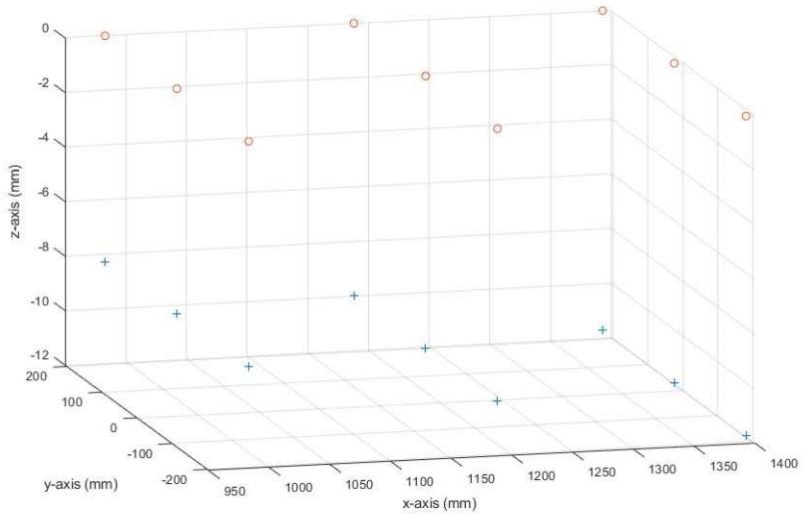

Figure 4.2: The Points A-H and O of the real (+) and ideal (o) detector at a gantry angle of 0°in the new detector coordinate system.

Edge Point	ideal positions		before correction		after correction	
	x (px)	y (px)	x (px)	y(px)	x (px)	y(px)
E1	600	600	586	586	583	583
E2	4400	600	4414	586	4382	583
E3	600	4400	581	4419	582	4383
E4	4400	600	4419	4419	4383	4383

Table 4.1: In the first two columns the positions of the edge points of an image simulating an ideal detector having 5000x5000 px are listed. Afterwards the positions of the edge points of the image simulating an acquisition at a gantry angle of 0°and having 5000x5000 px before correction and 4958x4943 px after correction are listed.

Edge Points	before correction		after correction		distortion (px)	
	x (px)	y (px)	x (px)	y (px)	before correction	after correction
E3-E1	-5	3831	-1	3800	-5/0	-1/0
E2-E1	3828	0	3799	0	0/0	0/0
E4-E2	5	3831	1	3800	5/0	1/0
E4-E3	3838	0	3801	0	0/0	0/0

Table 4.2: The differences between the edge points before and after application of the correction algorithm. The last two columns show the experienced distortions before and after correction.

Name	Gantry angle 0°		Gantry angle 180°	
	x (px)	y (px)	x (px)	y(px)
A	56.88	951.57	43.25	950.12
B	72.07	39.71		
C	511.06	506.12	494.86	510.57
D	975.83	66.29	960.56	73.58
E	977.22	951.26	955.49	953.25

Table 4.3: The centre of the spheres presented in Figures 4.3a and 4.3b calculated in Matlab for gantry angles 0° and 180°. A-E represent the centres of the spheres.

4.3a. Moreover, one can see in Fig. 4.3a and Fig. 4.3b that the upper left spheres were further up than the upper right spheres. Additionally, a difference image was computed with the acquired images, shown in Fig. 4.4a. The mean difference of the intensity values of the area around the upper right sphere is calculated being -1491.8, while the minimum difference of the intensity values -5936 and the maximum is 3914.
The two acquired images are then used as an input to the corrective algorithm. In addition, the gantry angles and the detector position, in this case the isocentric position, are taken into account to retrieve the corresponding transformation matrices. Fig. 4.3c and Fig. 4.3d show the resulting images after the transformation matrices are applied onto the images. A difference image and the coordinates of the centres of the spheres are computed for the corrected and uncorrected images. The difference image of the corrected images is shown in Fig. 4.4b and the coordinates are computed as well. The mean difference of the intensity values of the upper right sphere is calculated being -1268.5, while the minimum differences is -5776 and the maximum 3613. To compare the coordinates of centres of the spheres, their differences are computed and are listed in table 4.4. The coordinates of each sphere of the image acquired at gantry angle 0° is subtracted by the coordinates of the same sphere calculated from the image acquired at gantry angle 180°. Additionally, the length of the distances between the centres measured at the images acquired at gantry angles 0° and 180° are computed before and after correction. It has to be noted, that the corrected images have different sizes than the images acquired by the Linac due to the transformation. These size differences are considered in the calculation of the distances between the coordinates of the spheres. Table 4.5 show how much the differences of the centres of the spheres changed in the x- and y-direction after correction. A negative difference means that the centres of the spheres at the images acquired at gantry angles 0° and

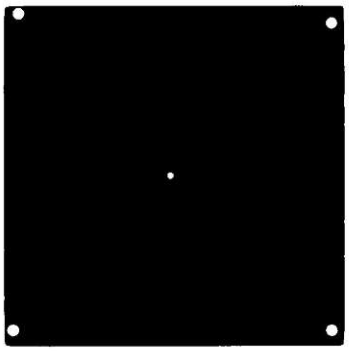

(a) An image acquired at a gantry angle of 0°.

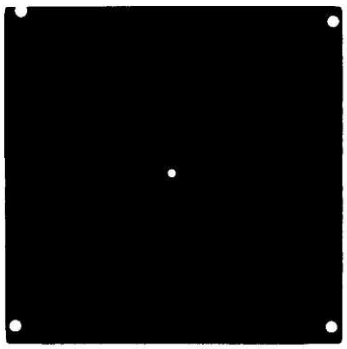

(b) An image acquired at a gantry angle of 180°.

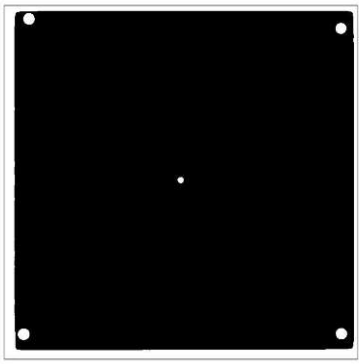

(c) This image shows the corrected image acquired at a gantry angle at 0°.

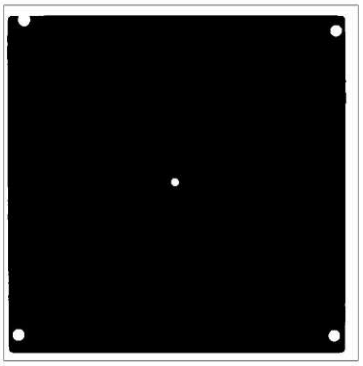

(d) This image shows the corrected image acquired at a gantry angle at 180°.

Figure 4.3: Images acquired at gantry angles 0° and 180° before and after correction turned into binary images and presenting 5 spheres located at the treatment table.

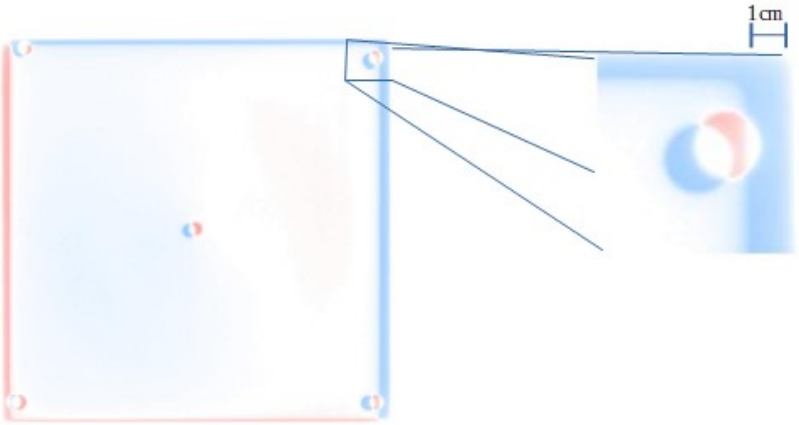

(a) This image shows the difference of the acquired images.

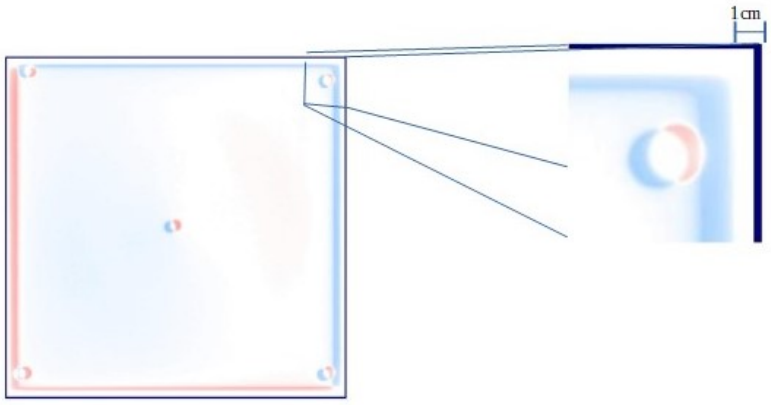

(b) This image shows the difference of the corrected images.

Figure 4.4: The difference of the images, which are acquired at gantry angles 0° and 180°with an image section from the upper right corner magnified. Blue shows a negative difference, red a positive one. The differences of the sphere in the magnified section is corrected by 5.48x5.56 px. 9.86x1.76 px remain to correct.

Name	before correction			after correction		
	x (px)	y (px)	length (px)	x (px)	y (px)	length (px)
A	13.69	1.45	13.76	19.22	-3.5	19.53
C	16.27	4.47	16.87	16.63	-4.38	17.19
D	15.34	-7.32	16.99	9.86	-1.76	10.01
E	21.82	-2	21.91	16.28	-7.51	17.92

Table 4.4: The differences of the centres of the spheres A,C, D and E taken at gantry angles of 0° and 180° and the lengths of these differences before and after correction. This indicates how far the centres are apart between 0° and 180°. The differences before correction were modified, as the images before and after correction have different sizes. The unit of measurements are pixels and therefore the length is the pixel length. The differences of the centre of sphere B is missing, as B is not recognised as an individual object by Matlab at the image acquired at gantry angle 180°. Consequently no difference can be calculated.

180°, are closer together in the considered direction before correction than after correction. A positive difference in table 4.5 means that the centres of the spheres at the images acquired at gantry angles 0° and 180° are closer together in the considered direction after correction than before correction.

Name	differences	
	x (px)	y (px)
A	-5.53	-2.05
C	-0.36	0.09
D	5.48	5.56
E	5.54	-5.51

Table 4.5: The differences of the differences of the centres of spheres calculated before and after correction. These differences are calculated by the absolute differences of the differences listed in table 4.4. A negative difference in this current table indicates that the centres of the spheres are further apart in the relevant direction, a positive change indicates that the centres of the spheres are nearer in the relevant direction.

5 Discussion

The starting point of this work was a tilted detector caused by gravity acquiring distorted images with the aim of developing a correction algorithm for improving images. A foregoing work [9] measured and calculated the deflection of the detector.
The results of this work showed an improvement of the image distortions caused by the deflection of the detector. Testing of the algorithm (chapter 4.1) showed that the calculation of the ideal detector centres resulted in a wanted semi-circle. Furthermore, no outliers were detected while plotting the ideal and real detectors as shown in Fig. 4.2. This indicated that the calculation of the points return reasonable results.
The edge points of the simulated image indicate a distortion in the image resulting in a shape of a trapeze instead of a rectangle, having a distortion of (10/0)px. After applying the transformation matrix the corresponding edges have an overall difference of (2/0)px, or 20% of the difference before correction. This remaining difference can be explained by an interpolation inaccuracy of the function applying the transformation matrix onto the image as nearest-neighbour interpolation is used for simplicity. Even with consideration of the remaining difference the application of the transformation matrix shows an improvement.
Two images were acquired at the Linac for validating the algorithm. Assuming an ideal detector system, the comparison of the acquired images from gantry angles 0° and 180° should not have resulted in any differences. Nonetheless, in Fig. 4.4a the red and blue areas of the image display differences between the acquired images. In this image a frame could be seen, as the two images acquired at gantry angles 0° and 180° have different boundaries due to the detector tilt. Additionally, the single spheres show differences as well. The centres of spheres differ ranging from 13.76 to 21.91 in pixel lengths (table 4.4).
After applying the corrective algorithm still a difference persists, shown in Fig. 4.4b. The dark blue frame is due to the different image sizes of the corrected images. Taken into account that bigger differences lead to larger differences in the intensity values of the difference images an improvement can be shown compared to Fig. 4.4a, as the mean differences of the intensity values after correction is -1268.5 compared to -1491.8. Additionally the differences yield a broader spectrum before correction (-5936; 3914) compared to after correction (-5776; 3613) indicating that the intensity of an average pixel differs less after correction compared

to before correction. An improvement can be seen in the table of the differences of coordinates as well. In table 4.4 still differences in coordinates of the centre of spheres persist, now having a difference in pixel lengths ranging from 10.01 to 19.53 and,having an average shortening of 1.22 pixels contrary to before correction (Table 4.4), which means that the centres of spheres after correction are closer together than before correction. The differences before and after correction of the differences of the centres of spheres of for example Point D listed in table 4.5 show an improvement in x- and y-direction, while Point E only shows an improvement in the x-direction. The changes of x- and y-directions in table 4.5 joined together reveal an improvement of the images as well. Yet, it can be seen, that the corrective algorithm improves better in the x-direction than in the y-direction. Overall, table 4.4 reveals a shortening in lengths of the differences between the coordinates of the centres of spheres of the two images after correction.
As the algorithm showed an improvement, but no eradication of the differences, the work is limited by some circumstances. Firstly, the distances from the isocentre to the detector centre were calculated for every 30° and not for every gantry angle, which can cause interpolation errors or inaccuracies for gantry angles in between. Furthermore, these distances were measured with an inclinometer, which lead to an increase of inaccuracy. The accuracy of this algorithm can be increased by measurements of the distances done by a more accurate method than with an inclinometer, such as an optical tracking tool. Furthermore, the frequency of the measurements can be increased, so that the measurement are done for every gantry angle. Here, it has to be compared and weighted how much effort has to be put into these measurements with how much the accuracy increases. Finally, the algorithm is written with the assumption, that the detector system as a whole bends linearly downwards due to gravity. As soon as the detector bends in a second direction or bends non-linearly the inaccuracy of the algorithm increases. In the foregoing work [9] measurements led to results which support the hypothesis that the detector bends along the y-axis as well, decreasing the accuracy of the correction algorithm applied onto the acquired images at the Linac. The fact that the corrective algorithm improves more in the x-direction than in the y-direction reinforce this hypothesis.

The so called gantry sag, the bending of the detector is well known. A study showed that due to the gantry sag the source-to-detector distance (SDD) changed for up to 7.5 mm at a Siemens Linac and the tilt value was under 1°[49].
Another study quantified the impact of isocentric shifts on delivery accuracy with two Elekta Synergy Linacs. They included amongst others gantry sag and distance of collimator as parameters in the study and concluded that the deviations diminished the accuracy. For quantification and correction of the deviations ad-

justments of beam isocentres in the Treatment Planning System (TPS) was used [50].
A different study conducted in 2012 measured the gantry sag at the Varian Linacs and performed correction depending on gantry angles to MLC leaf positions. The successful correction is limited in this study to a fixation of the collimator at 90°[5]. Another study investigated the gantry sag on Elekta Linacs. The largest SDD was found to be 12.9 mm, while the accepted criterion is 5 mm. When used for absolute dosimetry the increased SDD resulted in a 0.65% change of dose. This study also showed that the gantry sag has different values in-plane and cross-plane [51]. Different studies exist, which show that the mechanics of many Linacs lead to imperfect imaging. After different effects have been measured, different methods for corrections were used (e.g. correction in TPS or correction of MLC leaf position). In the present work measurements of the EPID and isocentre to detector distance were taken into account to develop an correction algorithm.

Another imaging system on the Linac is a kV-detector system with its detector arm mounted on the gantry as well. As the detector arms are constructed in a similar way it can be assumed that they behave similar as well. As a consequence the kV-detector would bend similarly due to gravity. Further measurements in this area may be considered as useful follow-up actions. Depending on the results of these measurements a similar algorithm might be necessary to correct the measured distortions. Another way to correct these distortions would be by mechanically stabilizing the detector. This has to be done by the manufacturer and not by the user.

6 Conclusion and Outlook

The developed algorithm written to correct the distortion in images acquired by the Linac shows a reduction of the distortion at the simulated images by 80%. The images acquired by the Linac for validation show an improvement after application of the correction algorithm, whereby the algorithm improves better in the x-direction than in the y-direction. This fact and data from a foregoing work support the hypothesis that the detector experiences a tilt in the y-direction too, which is not considered in this work.
On the gantry of the Linac a kV-detector system, another imaging system, is mounted. As its detector arm is constructed similar to the detector arm of the iVieGT™ detector, it can be assumed that it experiences a comparable tilt as well. This tilt would also lead to a distortion in images. Yet, further investigation is needed to determine the tilt of the kV-detector arm.

Bibliography

[1] S. Matsuhashi and N. S. Ishioka. "Medical Utilization of Radiation". In: *Radiation Applications. An Advanced Course in Nuclear Engineering*. Ed. by H. Kudo. Vol. 7. 2018. Chap. 17, pp. 293–332. DOI: https://doi.org/10.1007/978-981-10-7350-2_17.

[2] N. Suntharalingam, E.B. Podgorsak, and H. Tölli. "Brachytherapy: Physical and Clinical Aspects". In: *Radiation Oncology Physics: A Handbook for Teachers and Students*. Ed. by E.B. Podgorsak. IAEA, 2005. Chap. 13.

[3] E.B. Podgorsak. "Treatment Machines for External Beam Radiotherapy". In: *Radiation Oncology Physics: A Handbook for Teachers and Students*. Ed. by E.B. Podgorsak. IAEA, 2005. Chap. 5.

[4] P. Winkler et al. "Dose-response characteristics of an amorphous silicon EPID". In: *Med. Phys.* (2005). DOI: 10.1118/1.2040711.

[5] W. et al Du. "Quantifying the gantry sag on linear accelerators and introducing an MLC-based compensation strategy". In: *Med Phys* (2012).

[6] Rowshanfarzad P. et al. "An EPID-based method for comprehensive verification of gantry, EPID and the MLC carriage positional accuracy in Varian linacs during arc treatments". In: *Radiation Oncology* (2014).

[7] Riis H. et al. "Gantry and isocenter displacements of a linear accelerator caused by an add-on multileaf collimator". In: *Med Phys* (2013).

[8] Jin G. et al. "Gantry angledependent correction of dose detection error due to panel position displacement in IMRT dose verification using EPIDs". In: *Phys Med* (2014).

[9] Armando Aldy Ruddyard. "Charakterisierung der Detektorbewegung eines Linearbeschleunigers". Master thesis. Atomic institue of the physics faculty of the Technical University Vienna, 2020.

[10] M. Beyzadeoglu et al. "Radiobiology". In: *Basic Radiation Oncology*. 2010. DOI: 10.1007/978-3-642-11666-7_2.

[11] World Health Organization Internation Agency for Research on Cancer. *Latest global cancer data: Cancer burden rises to 18.1 million new cases and 9.6 million cancer deaths in 2018*. Press Releease No. 263. 2018.

[12] T. Q. Huynh et al. "An Overview of Immune Checkpoints and Immunotherapy in Cancer". In: *7th International Conference on the Development of Biomedical Engineering in Vietnam (BME7)*. Ed. by Vo Van Toi et al. Singapore: Springer Singapore, 2020, pp. 619–625. ISBN: 978-981-13-5859-3.

[13] M. Beyzadeoglu et al. "Clinical Radiation Oncology". In: *Basic Radiation Oncology*. 2010. DOI: 0.1007/978-3-642-11666-7_3.

[14] S. Poty. "α-Emitters for Radiotherapy: From Basic Radiochemistry to Clinical Studies—Part 1". In: *THE JOURNAL OF NUCLEAR MEDICINE* 59.6 (2018).

[15] Adriano Marcolongo et al. "Risks in Oncology and Radiation Therapy". In: *Textbook of Patient Safety and Clinical Risk Management*. Ed. by Liam Donaldson et al. 2021.

[16] Neil G Burnet et al. "Defining the tumour and target volumes for radiotherapy". In: *Cancer Imaging* 4 (2004), pp. 153–161. DOI: 10.1102/1470-7330.2004.0054.

[17] T. Landberg et al. "Report 50". In: *Journal of the International Commission on Radiation Units and Measurements* os26.1 (Apr. 2016), NP–NP. ISSN: 1473-6691. DOI: 10.1093/jicru/os26.1.Report50. eprint: https://academic.oup.com/jicru/article-pdf/os26/1/NP/9587111/jicruos26-NP.pdf. URL: https://doi.org/10.1093/jicru/os26.1.Report50.

[18] T. Landberg et al. "Report 62". In: *Journal of the International Commission on Radiation Units and Measurements* os32.1 (Apr. 2016), NP–NP. ISSN: 1473-6691. DOI: 10.1093/jicru/os32.1.Report62. eprint: https://academic.oup.com/jicru/article-pdf/os32/1/NP/9587475/jicruos32-NP.pdf. URL: https://doi.org/10.1093/jicru/os32.1.Report62.

[19] N. Hodapp. "Der ICRU-Report 83: Verordnung, Dokumentation und Kommunikation der fluenzmodulierten Photonenstrahlentherapie (IMRT)". In: *Strahlentherapie und Onkologie* 188.1 (Jan. 1, 2012), pp. 97–100. ISSN: 1439-099X. DOI: 10.1007/s00066-011-0015-x. URL: https://doi.org/10.1007/s00066-011-0015-x.

[20] Lotte Wilke et al. "ICRU report 91 on prescribing, recording, and reporting of stereotactic treatments with small photon beams". In: *Strahlentherapie und Onkologie* 195.3 (Mar. 1, 2019), pp. 193–198. ISSN: 1439-099X. DOI: 10.1007/s00066-018-1416-x. URL: https://doi.org/10.1007/s00066-018-1416-x.

[21] H. Wiedemann. “Introduction to Accelerator Physics”. In: *Particle Accelerator Physics*. Springer International Publishing, 2015.

[22] E.B. Podgorsak (Technical Editor). *Radiation Oncology Physics: A Handbook for Teachers and Students*. IAEA, 2005.

[23] Wilfried De Neve. “Rationale of Intensity Modulated Radiation Therapy: A Clinician’s Point of View”. In: *Image-Guided IMRT*. Ed. by Thomas Bortfeld et al. 2006. Chap. 1.

[24] W. Schlegel. “Bestrahlungsgeraete der Teletherapie”. In: *Medizinische Physik*. Ed. by W. Schlegel. Ed. by C.P. Karger. Ed. by O. Jäkel. 2018.

[25] Elekta Limited. *Elekta Medical Linear Accelerator. Site Planning Construction Information*. 2014.

[26] S.H. Levitt et al. *Technical Basis of Treatment Therapy. Practical Clinical Applications*. Ed. by S. H. Levitt. Ed. by J. A. Purdy. Ed. by C. A. Perez. Ed. by S. Vijayakumar. 4th ed. Springer-Verlag Berlin Heidelberg, 2006.

[27] Asghar Mesbahi. “Development a simple point source model for Elekta SL-25 linear accelerator using MCNP4C Monte Carlo code”. In: *J. Radiat. Res* 4 (Jan. 2006), pp. 7–1.

[28] Haim Azhari et al.

[29] M. Beyzadeoglu et al. “Radiation Physics”. In: *Basic Radiation Oncology*. 2010. DOI: 10.1007/978-3-642-11666-7_1.

[30] J. Wetzl F. Lugauer. “Magnetic Resonance Imaging”. In: *Medical Imaging Systems. An Introductory Guide*. Ed. by A. Maier. Ed. by St. Steidl. Ed. by V. Christlein. Ed. by J. Hornegger. Springer open, 2018. Chap. 6.

[31] A. Berger. “Magnetic resonance imaging”. In: *The BMJ* (2002).

[32] W. Schlegel. *Medizinische Physik: Grundlagen – Bildgebung – Therapie – Technik*. Springer Berlin Heidelberg, 2018. ISBN: 9783662548004. URL: https://books.google.at/books?id=aucTtAEACAAJ.

[33] J. Sanders. “Emission Tomography”. In: *Medical Imaging Systems. An Introductory Guide*. Ed. by A. Maier. Ed. by St. Steidl. Ed. by V. Christlein. Ed. by J. Hornegger. Springer open, 2018. Chap. 10.

[34] Luc Bidaut et al. “Imaging in Radiation Oncology”. In: *Leibel and Phillips Textbook of Radiation Oncology*, 3rd ed. Philadelphia: W.B. Saunders, 2010. Chap. 8, pp. 120–154. ISBN: 978-1-4160-5897-7. DOI: https://doi.org/10.1016/B978-1-4160-5897-7.00008-1. URL: https://www.sciencedirect.com/science/article/pii/B9781416058977000081.

[35] J. Vince. *Mathematics for Computer Graphics*. 2010.

[36] Th. B. Moeslund. "Geometric Transformations". In: *Introduction to Video and Image Processing: Building Real Systems and Applications*. London: Springer London, 2012, pp. 141–153. ISBN: 978-1-4471-2503-7. DOI: 10.1007/978-1-4471-2503-7_10. URL: https://doi.org/10.1007/978-1-4471-2503-7_10.

[37] J.-H. Park et al. "Fresnel and Fourier hologram generation using orthographic projection images". In: *Optics Express. Optical Society of America* (2009).

[38] J.-H. Park et al. "View image generation in perspective and orthographic projection geometry based on integral imaging". In: *Optics Express. Optical Society of America* (2008).

[39] Zhiping Mu. "A Fast DRR Generation Scheme for 3D-2D Image Registration Based on the Block Projection Method". In: June 2016, pp. 609–617. DOI: 10.1109/CVPRW.2016.82.

[40] George W. Sherouse, Kevin Novins, and Edward L. Chaney. "Computation of digitally reconstructed radiographs for use in radiotherapy treatment design". In: *International Journal of Radiation Oncology*Biology*Physics* 18.3 (1990), pp. 651–658. ISSN: 0360-3016. DOI: https://doi.org/10.1016/0360-3016(90)90074-T. URL: https://www.sciencedirect.com/science/article/pii/036030169090074T.

[41] Kiaran McGee, Indra Das, and Colin Sims. "Evaluation of digitally reconstructed radiographs (DRRs) used for clinical radiotherapy: A phantom study". In: *Medical physics* 22 (Nov. 1995), pp. 1815–27. DOI: 10.1118/1.597637.

[42] Ganesh Narayanasamy et al. "Commissioning an Elekta Versa HD linear accelerator". In: *Journal of Applied Clinical Medical Physics* 17 (Jan. 2016), p. 179. DOI: 10.1120/jacmp.v17i1.5799.

[43] Elekta Limited. *iViewGT™. User Manual*. 2006.

[44] Elekta. *Elekta Medical Linear Accelerator iViewGT™ R3.4.1 Instructions for Use for: Precise Digital Accelerator, Elekta Synergy® Platform, Elekta Synergy®, Elekta Infinity™, Elekta Axess™, and Versa HD™*. 2015.

[45] P. Winkler and D. Georg. "An intercomparison of 11 amorphous silicon EPIDs of the same type: implications for portal dosimetry". In: *Phys. Med. Biol.* (2006). DOI: 10.1088/0031-9155/51/17/005.

[46] Inc The MathWorks, ed. *Matlab*. retrieved on January 28th, 2021. URL: https://de.mathworks.com/products/matlab.html.

[47] The Mathworks Inc. *fitgeotrans*. retrieved on OCtobre 3rd, 2021. URL: https://de.mathworks.com/help/images/ref/fitgeotrans.html.

[48] The Mathworks Inc. *imwarp*. retrieved on OCtobre 3rd, 2021. URL: `https://de.mathworks.com/help/images/ref/imwarp.html`.

[49] Pejman Rowshanfarzad et al. "Investigation of the mechanical performance of Siemens linacs components during arc: gantry, MLC , and electronic portal imaging device". In: *Medical Devices: Evidence and Research* (2015).

[50] Linda Wack. "The impact of isocentric shifts on delivery accuracy during the irradiation of small cerebral targets—Quantification and possible corrections". In: *Applied Clinical Medical Physics* (2020).

[51] P Rowshanfarzad et al. "A comprehensive study of the mechanical performance of gantry, EPID and the MLC assembly in Elekta linacs during gantry rotation." In: *The British Journal of Radiology* (2015).